nature neuroscience

Ca^{2+} signaling in astrocytes from *Ip3r2*$^{-/-}$ mice in brain slices and during startle responses *in vivo*

Rahul Srinivasan[1,7], Ben S Huang[2,7], Sharmila Venugopal[1], April D Johnston[1], Hua Chai[1], Hongkui Zeng[3], Peyman Golshani[2,4,5] & Baljit S Khakh[1,6]

Intracellular Ca^{2+} signaling is considered to be important for multiple astrocyte functions in neural circuits. However, mice devoid of inositol triphosphate type 2 receptors (IP3R2) reportedly lack all astrocyte Ca^{2+} signaling, but display no neuronal or neurovascular deficits, implying that astrocyte Ca^{2+} fluctuations are not involved in these functions. An assumption has been that the loss of somatic Ca^{2+} fluctuations also reflects a similar loss in astrocyte processes. We tested this assumption and found diverse types of Ca^{2+} fluctuations in astrocytes, with most occurring in processes rather than in somata. These fluctuations were preserved in *Ip3r2*$^{-/-}$ (also known as *Itpr2*$^{-/-}$) mice in brain slices and *in vivo*, occurred in end feet, and were increased by G protein–coupled receptor activation and by startle-induced neuromodulatory responses. Our data reveal previously unknown Ca^{2+} fluctuations in astrocytes and highlight limitations of studies that used *Ip3r2*$^{-/-}$ mice to evaluate astrocyte contributions to neural circuit function and mouse behavior.

Astrocytes are found throughout the brain and possess thousands of processes in well-delineated astrocyte territories[1,2] that form the anatomical basis for interactions with neurons, other glia and blood vessels[3]. A major open question in neuroscience concerns how astrocytes contribute to the functioning of the brain and to neurological and psychiatric disorders[4]. From this perspective, much attention has focused on the existence and physiological function(s) of astrocyte intracellular Ca^{2+} signals[5], which we refer to as Ca^{2+} fluctuations.

Early studies showed that astrocytes displayed intracellular Ca^{2+} fluctuations that were both spontaneous and triggered by neurotransmitters[6]. Subsequently, organic Ca^{2+} indicator dyes have been used extensively to study astrocyte Ca^{2+} fluctuations in brain slices and *in vivo* during various types of pharmacological and sensory stimuli (reviewed in refs. 5,7). In these settings, Ca^{2+} fluctuations were used in a correlative manner with simultaneous measurements from neurons or the vasculature. On the basis of such experiments, evidence indicates that astrocyte Ca^{2+} fluctuations occur during neurotransmitter release and affect neuronal[8] and neurovascular functions[3]. Taken together, these studies suggest that astrocytes contribute to information processing and neurovascular coupling in addition to their trophic and supportive roles.

Several recent studies have questioned the physiological importance of astrocyte Ca^{2+} signaling based in large part on the use of genetically modified mice in which Ca^{2+} fluctuations were reported to be completely absent in all astrocytes[9–11]. In such studies, the genetic deletion of inositol triphosphate type 2 receptor (IP3R2), which is known to be enriched in astrocytes[12], led to the apparent loss of all astrocyte Ca^{2+} fluctuations, but had no effect on behavioral[13], neuronal[9,10] or vascular functions[14–16], leading the authors to conclude that astrocyte Ca^{2+} fluctuations have no role in these functions. However, other studies utilizing similar or complementary approaches have suggested that astrocyte Ca^{2+} fluctuations are involved in blood vessel and neuronal functions[17–21]. Overall, a confusing picture has emerged on astrocyte intracellular Ca^{2+} fluctuations and their physiological relevance.

We set out to test the assumption that all astrocyte Ca^{2+} fluctuations are abolished in *Ip3r2*$^{-/-}$ mice. We employed fast genetically encoded Ca^{2+} indicators[22] that can be selectively expressed in astrocytes and not in other cells[23,24] without causing astrocyte reactivity in the hippocampus[23,24], striatum[25] or cortex[16]. We also used adult mice[26] and studied astrocytes in hippocampal slices to be concordant with past work[9,10]. To avoid the complications caused by anesthesia[27,28], we used two-photon microscopy to study astrocytes in awake, non-anesthetized, head-fixed mice that were free to rest or run on a treadmill. Using this procedure, we assessed how astrocytes responded during startle responses mediated by endogenous norepinephrine release[29,30]. Finally, we employed objective, semi-automated and standardized data analyses using newly developed software. The combination of these approaches revealed that Ca^{2+} fluctuations were not abolished in astrocytes in *Ip3r2*$^{-/-}$ mice as previously thought. Rather, we found a rich variety of previously unknown IP3R2-independent Ca^{2+} fluctuations in astrocyte processes that responded to pharmacological and sensory stimuli in brain slices and *in vivo*, respectively.

[1]Department of Physiology, David Geffen School of Medicine, University of California Los Angeles, Los Angeles, California, USA. [2]Department of Neurology, David Geffen School of Medicine, University of California Los Angeles, Los Angeles, California, USA. [3]Allen Institute for Brain Science, Seattle, Washington, USA. [4]Integrative Center for Learning and Memory, David Geffen School of Medicine, University of California Los Angeles, Los Angeles, California, USA. [5]West Los Angeles VA Medical Center, Los Angeles, California, USA. [6]Department of Neurobiology, David Geffen School of Medicine, University of California Los Angeles, Los Angeles, California, USA. [7]These authors contributed equally to this work. Correspondence should be addressed to B.S.K. (bkhakh@mednet.ucla.edu).

Received 29 January; accepted 15 March; published online 20 April 2015; doi:10.1038/nn.4001

RESULTS

Astrocyte spontaneous Ca^{2+} fluctuations in hippocampal slices from *Ip3r2*$^{-/-}$ mice

We used adeno-associated virus (AAVs) of the 2/5 serotype and the minimal astrocyte-specific *GfaABC$_1$D* promoter to express cytosolic GCaMP6f in astrocytes located in the CA1 region of the adult mouse hippocampus[23,24]. We harvested hippocampal slices 2 weeks after *in vivo* virus microinjections, identified single GCaMP6f-expressing astrocytes and imaged Ca^{2+} fluctuations with confocal microscopy from wild-type (WT) and *Ip3r2*$^{-/-}$ mice (n = 5 mice of each genotype; **Supplementary Videos 1** and **2**). GCaMP6f imaging revealed a large number of Ca^{2+} fluctuations in astrocytes, more than previously observed with organic Ca^{2+} indicator dyes[9,10,23,31,32], illustrating the utility of GCaMP6f[22]. To analyze Ca^{2+} fluctuations identically and objectively for all cells, we developed GECIquant software that permits rapid semi-automated detection of regions of interest (ROIs) containing Ca^{2+} fluctuations (**Supplementary Fig. 1**). GECIquant performed a series of user-instigated pixel operations for maximum intensity projection, background subtraction, object thresholding, measurement of object areas, object centroids and distance of the object to the somatic centroid (**Supplementary Fig. 1a–f** and **Supplementary Code**). GECIquant was rigorously tested for its ability to faithfully identify, measure (**Supplementary Fig. 2**), trace (**Supplementary Fig. 3**) and track fluorescence fluctuations (**Supplementary Fig. 4**) using fluorescent beads, morphologically complex cells and blinking quantum dots (**Supplementary Figs. 1–4**). After optimization, we used GECIquant to study GCaMP6f-expressing astrocytes (**Supplementary Fig. 1g**) that were separated from surrounding GCaMP6f-expressing astrocytes, that is, we focused on single cells. This was possible because of the documented sparse nature of GCaMP

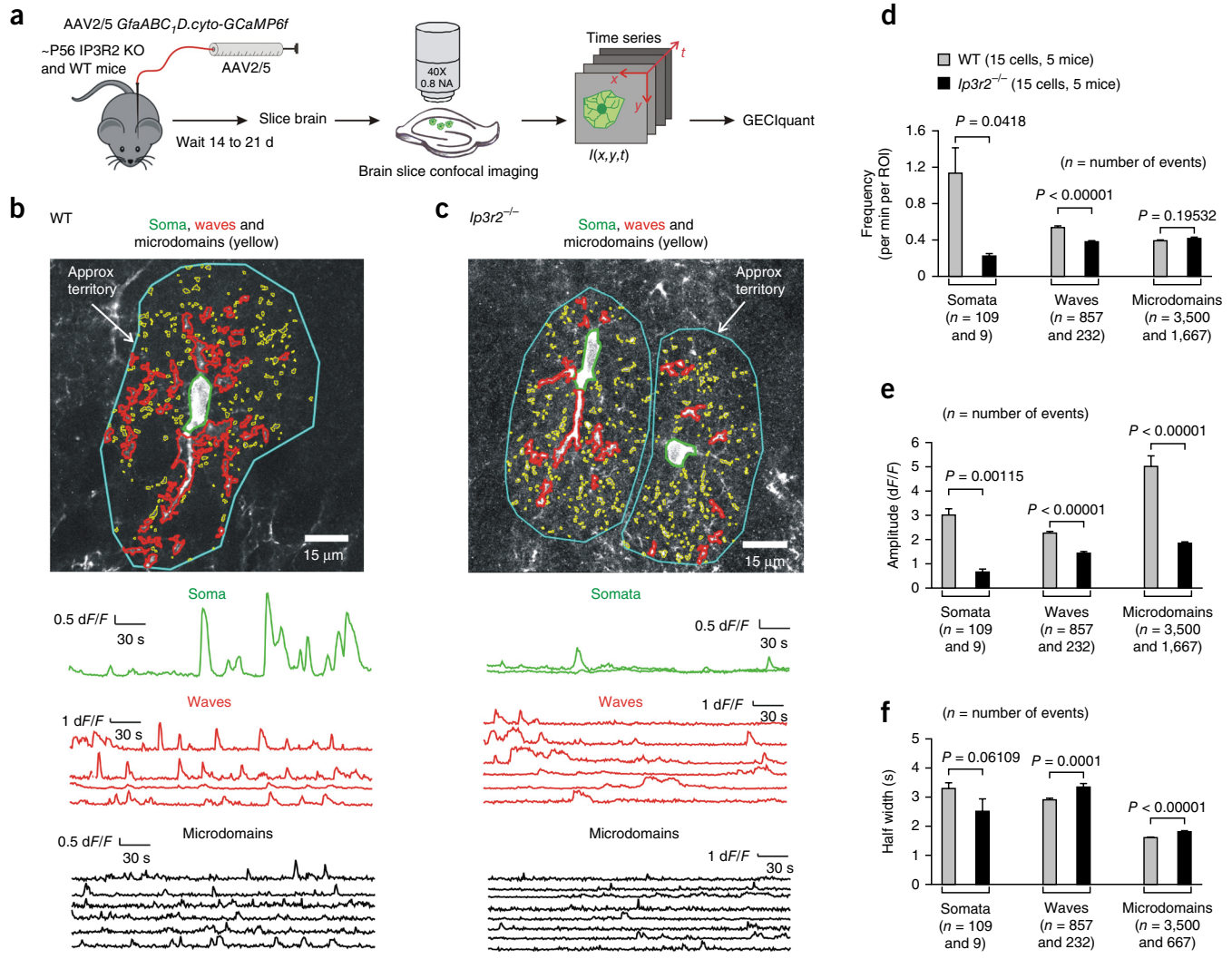

Figure 1 Ca^{2+} fluctuations in hippocampal astrocytes from WT and *Ip3r2*$^{-/-}$ mice. (**a**) Schematic illustrating the experimental approach. (**b**) Representative images and traces for Ca^{2+} fluctuations measured in an astrocyte from a WT mouse. Three predominant types of Ca^{2+} events are demarcated: somatic fluctuations (green), waves (red) and microdomains (yellow). Approximate territory boundaries are outlined in blue, but these were not used for data analyses and are shown only for illustrative purposes. (**c**) Data are presented as in **b**, but for two astrocytes from an *Ip3r2*$^{-/-}$ mouse. Representative movies are shown as **Supplementary Videos 1** and **2**. (**d–f**) Average data for Ca^{2+} fluctuation properties in WT and *Ip3r2*$^{-/-}$ mice (n = 15 and 17 astrocytes WT and *Ip3r2*$^{-/-}$, and 5 mice for each). For this and all other figures, statistical comparisons were made using unpaired non-parametric Mann-Whitney or unpaired parametric Student's t tests as deemed appropriate after analyzing the raw data (Online Methods). The n numbers on **d–f** refer to the numbers of Ca^{2+} fluctuations for the WT and *Ip3r2*$^{-/-}$ bars, which were averaged for frequency, amplitude and half-width across all cells. The data are shown as mean ± s.e.m.

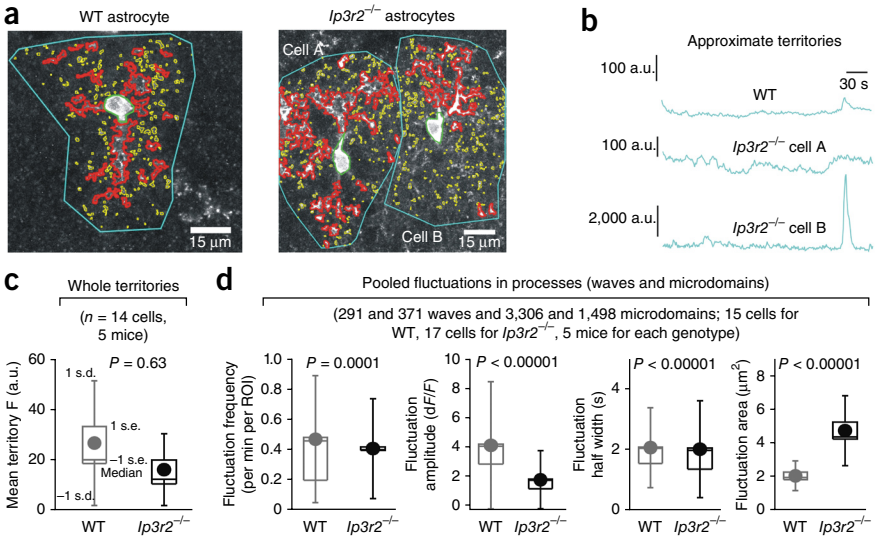

Figure 2 Ca^{2+} fluctuations within astrocyte processes are largely intact in brain slices from *Ip3r2*$^{-/-}$ mice. (**a**) Representative images of astrocytes from WT and *Ip3r2*$^{-/-}$ mice with somatic (green), wave (red) and microdomain (yellow) compartments demarcated in different colors. Approximate territory boundaries are outlined in blue, but were only used for analyses shown in **b** and **c**. (**b**,**c**) Representative traces for territory ROI fluctuations for the cells shown in **a**. Such traces were used to measure the average fluorescence over 300 s in **c**. Note that the drawing of the territory for this single specific data set (**b**) is approximate. (**d**) Summary data for WT and *Ip3r2*$^{-/-}$ mice for wave and microdomain fluctuations in astrocyte processes, plotted as box and whisker plots; note that these are pooled data from microdomains and waves.

expression using AAV2/5 and the *GfaABC$_1$D* promoter[23,24].

In the case of WT mouse astrocytes expressing GCaMP6f, we were able to readily identify somatic Ca^{2+} fluctuations, which by definition occurred in the anatomically well-defined cell body and covered an area of 80.4 ± 7.8 µm^2 (n = 109 somatic fluctuations, 15 cells, 5 mice). However, we also found numerous fluctuations in processes. One type of fluctuation in processes appeared as expanding and contracting local waves that spread between adjacent pixels; we refer to these as waves. The waves spread to an area of 14.8 ± 1.4 µm^2 and displayed average centroid distances of 26.4 ± 0.7 µm from the somatic centroid (n = 837 waves, 15 cells, 5 mice). The second type of Ca^{2+} fluctuations in processes, which we refer to as microdomains, were restricted in area to 0.7 ± 0.01 µm^2 and displayed average centroid distances of 29.2 ± 0.2 µm from the somatic centroid (n = 3,500 microdomains, 15 cells, 5 mice). Thus, the distinction between somatic fluctuations, waves and microdomains in processes was based on their detection using GECIquant (Online Methods), differences in their properties (**Fig. 1**), significant differences in the areas covered by the fluctuations (**Supplementary Fig. 5**), and their locations in astrocyte cell bodies or processes (**Supplementary Fig. 6**).

Once detected using GECIquant (**Fig. 1a**–**c**), we analyzed the numerous Ca^{2+} fluctuations in WT and *Ip3r2*$^{-/-}$ astrocytes and quantified their basic properties (**Fig. 1**). We found that, although the frequency (**Fig. 1d**), amplitude (**Fig. 1e**) and duration (**Fig. 1f**) of somatic Ca^{2+} fluctuations were significantly reduced in *Ip3r2*$^{-/-}$ mice, the fluctuations were clearly not abolished ($P < 0.05$ using unpaired Student's t tests; **Fig. 1b**–**f** and **Supplementary Video 2**). Moreover, we found only a subtle decrease in the frequency of waves, no change in the frequency of microdomains in processes (**Fig. 1d**) and a ~50–60% decrease in their amplitude that was accompanied by a significant increase in their duration ($P < 0.05$ using unpaired Student's t tests; **Fig. 1e**,**f**). Ca^{2+} waves and microdomains detected in processes were located at equivalent distances from the somata in WT and *Ip3r2*$^{-/-}$ mice (**Supplementary Fig. 5**). In addition, for the data shown in **Figure 1d**–**f**, the number of ROIs per cell were 19 ± 2 and 196 ± 18 for waves and microdomains, respectively, for WT mice. The equivalent numbers for ROIs per cell were 19 ± 2 and 72 ± 6 for waves and microdomains, respectively, for *Ip3r2*$^{-/-}$ mice. However, the data report frequency per ROI, and differences in the numbers of ROIs between genotypes therefore cannot explain the differences (**Fig. 1d**). Nonetheless, it should be noted that, although fewer microdomain ROIs were detected in *Ip3r2*$^{-/-}$ in relation to WT mice (72 ± 6 versus 196 ± 18), microdomain ROIs were clearly not abolished. These analyses showed that Ca^{2+} signaling was not completely absent in all hippocampal astrocytes as previously reported[9–11,33]. Moreover, from a population of 15 cells from 5 WT and 17 cells from 5 *Ip3r2*$^{-/-}$ mice we found that most Ca^{2+} fluctuations occurred in processes rather than the somata (**Fig. 1**). Thus, in WT mice, the overall numbers of Ca^{2+} fluctuations were 4.7 ± 1.6 and 37.7 ± 8.5 fluctuations per cell per min for somata and processes, respectively. In the case of *Ip3r2*$^{-/-}$ mice, the equivalent numbers were 0.5 ± 0.2 and 15.6 ± 3.6 fluctuations per cell per min for somata and processes, respectively. This is a notable discovery given that past evaluations using *Ip3r2*$^{-/-}$ mice have been based on measurement and quantification of somata alone[9–11,33].

To further verify our measurements, we performed one specific set of analyses to examine Ca^{2+} fluctuations in entire astrocytes by measuring the mean fluorescence intensity values for traces lasting 300 s. For this specific data set, ROIs that approximately encompassed entire astrocytes (that is, territories) were drawn (**Fig. 2a**,**b**); note that the drawing of territory ROIs was approximate and only used for the data set in **Figure 2c**. We reasoned that, if Ca^{2+} fluctuations were absent in *Ip3r2*$^{-/-}$ mice, then this analysis would reveal significantly lower mean fluorescence values over time in comparison to WT mice, where there was an abundance of Ca^{2+} fluctuations (**Fig. 1**). In contrast, we found no significant differences in mean fluorescence over 300-s-long traces between WT and *Ip3r2*$^{-/-}$ mice ($P = 0.63$ with an unpaired Mann-Whitney test; **Fig. 2c**), suggesting that, when averaged across entire astrocytes, fluctuations in astrocyte Ca^{2+} are largely preserved in *Ip3r2*$^{-/-}$ mice (**Fig. 2b**,**c**). A similar result was found when we pooled wave and microdomain fluctuations from processes (**Fig. 2d**). We found only subtle changes in frequency and duration of these pooled events (**Fig. 2d**). We did detect a halving of the amplitude in *Ip3r2*$^{-/-}$ mice ($P < 0.00001$ with an unpaired Mann-Whitney test; **Fig. 2d**). However, this was accompanied by an increase in the average area of pooled waves and microdomains per astrocyte in *Ip3r2*$^{-/-}$ mice (**Fig. 2d**). The areas of the individual types of Ca^{2+} fluctuations are shown in **Supplementary Figure 5.** Overall, the loss of IP3R2s resulted in substantial, but incomplete, loss of somatic Ca^{2+} fluctuations. In contrast, Ca^{2+} fluctuations in processes were still present and, when carefully assessed by several metrics, existed in clearly observable numbers in *Ip3r2*$^{-/-}$ mice (**Figs. 1** and **2**).

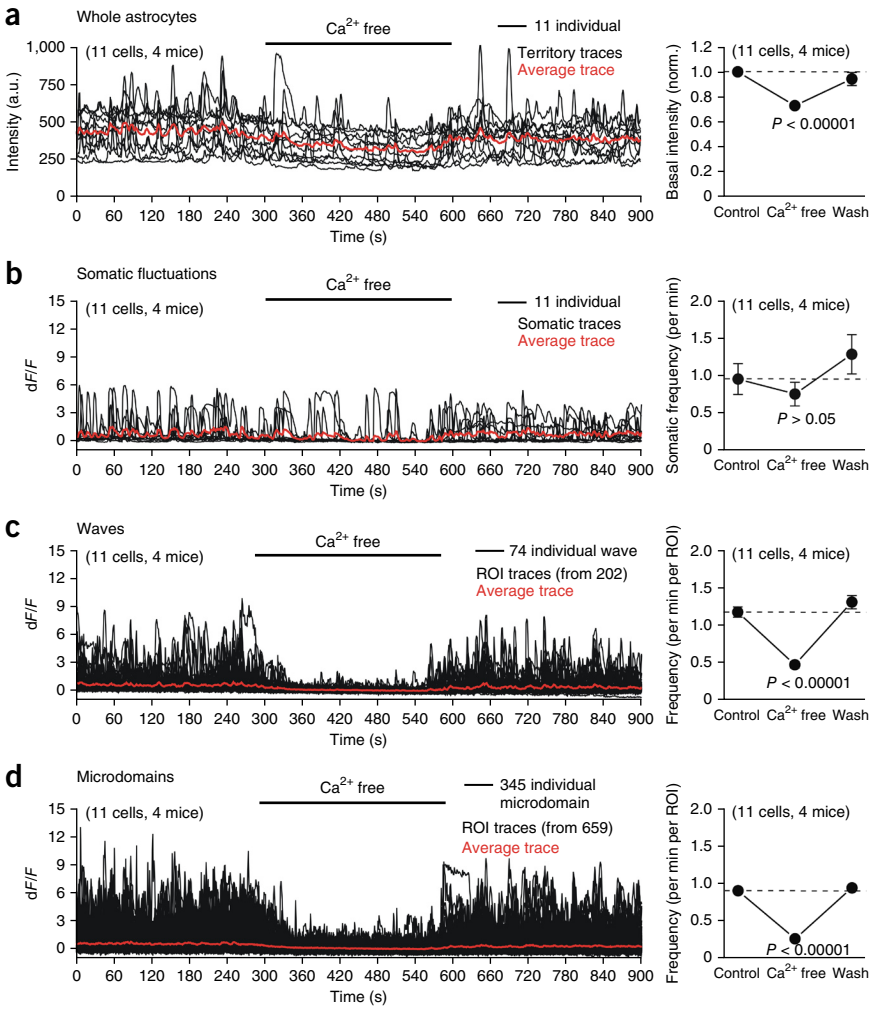

Figure 3 Effect of nominally Ca^{2+}-free buffer applications on astrocyte Ca^{2+} fluctuations in WT mice. (**a**) Traces and average data for the effect of nominally Ca^{2+} free buffers on the basal fluorescence intensity of ROIs corresponding approximately to entire astrocytes. (**b**–**d**) Data are presented as in **a**, but for somatic fluctuations (**b**) as well as for wave (**c**) and microdomain (**d**) fluctuations in astrocyte processes. The averages are across all cells for the ROIs indicated in each set of traces. The data are shown as mean ± s.e.m.

Notably, many Ca^{2+} fluctuations in processes were also seen in WT mice after depletion of intracellular Ca^{2+} stores with cyclopiazonic acid (CPA, $n = 10$ cells from 3 mice; **Supplementary Tables 1** and **2**). We next directly compared Ca^{2+} fluctuations observed in *Ip3r2*$^{-/-}$ mice with fluctuations in WT mice after CPA. Overall, these two data sets were similar, but not identical (**Supplementary Tables 1** and **2**). This may suggest the existence of subtle differences in the ability of CPA and *Ip3r2*$^{-/-}$ to unmask the signals that are not dependent on intracellular Ca^{2+} stores. However, the main point is that many signals can be observed in astrocyte processes of WT mice after depletion of stores with CPA, which recalls, but is not identical to, the *Ip3r2*$^{-/-}$ data (**Supplementary Tables 1** and **2**).

We next addressed the issue of whether the Ca^{2+} fluctuations we observed in single astrocytes (**Fig. 1**) may reflect some fluctuations emanating from other nearby astrocytes that also expressed GCaMP6f. This issue cannot be addressed by filling an astrocyte with a fluorescent dye via a patch pipette to demarcate its territory, as the dye will spread to ~50–200 neighboring astrocytes in the CA1 region in minutes via gap junction coupling[34–36] and thereby make the task of defining the boundaries of the patched cell even more problematic. Moreover, the act of patching an astrocyte is disruptive and leads to run down of Ca^{2+} fluctuations[37]. Finally, our past experiences using this approach[32] in relation to the use of GCaMP3 (ref. 23) showed that GCaMP3 was vastly superior. However, to address this issue, we compared our original data set that was gathered from single astrocytes to a specific set of astrocytes that were selected to be completely isolated from other GCaMP6f-expressing astrocytes (**Supplementary Fig. 7**), which was possible because of the sparse nature of GCaMP6f expression by AAV2/5 (ref. 24). We also compared both of these data sets to astrocytes from offspring of GCaMP6f^{flx} (*loxP*-flanked STOP cassette that prevents GCaMP6f transcription) mice crossed with *GLAST*-CreERT2 mice after tamoxifen induction[24]. In this genetic cross, only ~31% of astrocytes in the CA1 region expressed GCaMP6f, and ~37% of these were easily identified as isolated, which permitted assessment of Ca^{2+} fluctuations in isolated cells (**Supplementary Fig. 8**). If we had overestimated the frequency of Ca^{2+} fluctuations in our original data set (**Fig. 1**), then we would predict lower frequencies in the isolated astrocytes (from AAV2/5 injections and GCaMP6f^{flx} mice). In fact, we found no differences in the frequency of Ca^{2+} fluctuations across these three groups (**Supplementary Fig. 9**). These data are entirely consistent with detailed anatomical studies showing that astrocytes have extremely well delineated territories that overlap by only ~5% among adjacent cells[1,2] and that astrocytes in the CA1 region of mice do not possess long processes that extend beyond their individual territories[1,2].

Ca^{2+} fluctuations in astrocyte processes are partly dependent on transmembrane Ca^{2+} fluxes

Our data (**Figs. 1** and **2**) show that a component of astrocyte Ca^{2+} fluctuations is dependent on Ca^{2+} release from intracellular stores. We next explored how the Ca^{2+} fluctuations were affected by the application of nominally Ca^{2+} free buffers (**Fig. 3**). Application of Ca^{2+} free buffers reversibly reduced basal Ca^{2+} levels measured in entire astrocytes (**Fig. 3a**). However, Ca^{2+} free buffer applications did not significantly change the frequency of somatic Ca^{2+} fluctuations (**Fig. 3b**), which is consistent with the observation that somatic fluctuations were significantly reduced in the *Ip3r2*$^{-/-}$ mice (**Fig. 1**). In contrast, for 37 and 52% of wave and microdomain ROIs located in processes, Ca^{2+} free buffers reversibly reduced the Ca^{2+} fluctuation frequency (**Fig. 3c**,**d**). The frequencies of fluctuations in the remaining 63% of wave and 48% of microdomain ROIs were not markedly affected (**Supplementary Fig. 10**). These data suggest that transmembrane Ca^{2+} fluxes contribute substantially to basal Ca^{2+} levels and to a detectable proportion of waves and microdomains in processes (**Fig. 4**). Thus, mechanistically, both intracellular Ca^{2+} release (**Fig. 1**) and transmembrane entry (**Fig. 3**) underlie diverse Ca^{2+} fluctuations in astrocytes. It is interesting to

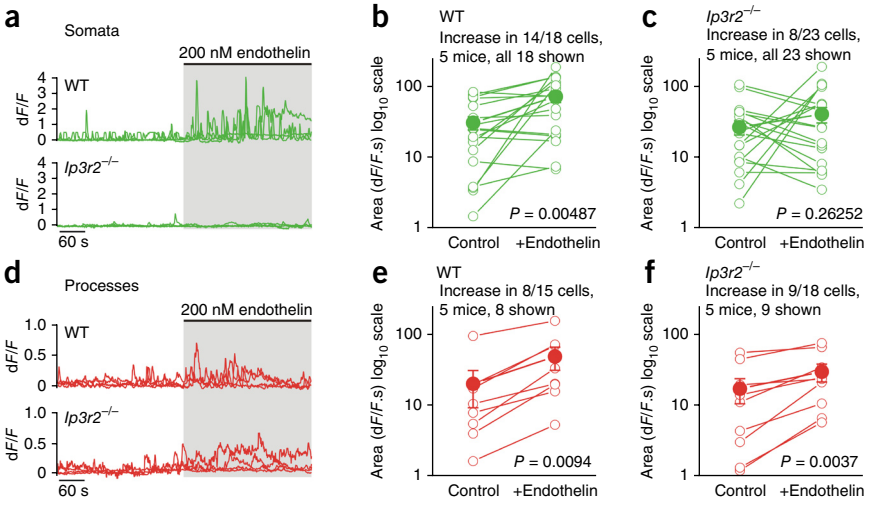

Figure 4 GPCR-mediated Ca^{2+} fluctuations in astrocyte processes are largely intact in hippocampal slices from *Ip3r2*$^{-/-}$ mice. (**a**–**c**) Representative traces and average data for endothelin-evoked Ca^{2+} fluctuations in astrocyte somata from WT and *Ip3r2*$^{-/-}$ mice. (**d**–**f**) Data are presented as in **a**–**c**, but for astrocyte processes. Five WT and five *Ip3r2*$^{-/-}$ mice were analyzed for these experiments, and paired Student's *t* tests were used when comparing before and during endothelin application. The data are shown as mean ± s.e.m.

note that the effect of Ca^{2+} free buffer on waves and microdomains was completely reversible, that is, the fluctuations returned to their normal levels almost exactly (**Fig. 3c**,**d**). Thus, Ca^{2+} fluctuations in processes are reproducible and stable over time.

GPCR-evoked Ca^{2+} fluctuations in astrocytes in hippocampal slices from *Ip3r2*$^{-/-}$ mice

We next used endothelin (200 nM) to activate Gq protein–coupled endothelin receptors (ETRs) on astrocytes to elicit Ca^{2+} elevations. We chose endothelin because it was used in past studies[10] and because RNA-seq analysis has shown that ETRs are enriched in astrocytes relative to neurons[12], thereby minimizing the potential complication of indirect actions via neurons for our evaluations. We measured strong endothelin-evoked intracellular Ca^{2+} fluctuations in the somata in 14 of 18 WT astrocytes. We quantified these data by measuring the areas under the traces before and during endothelin applications (**Fig. 4a**). When averaged across all 18 WT astrocytes, endothelin significantly elevated somatic Ca^{2+} levels ($P = 0.00487$, paired Student's *t* test; **Fig. 4b**). By repeating similar experiments with astrocytes from *Ip3r2*$^{-/-}$ mice, we found that endothelin failed to evoke significant somatic Ca^{2+} fluctuations from a population of 23 astrocytes ($P = 0.26252$, paired Student's *t* test; **Fig. 4c** and **Supplementary Videos 3** and **4**). However, it should be noted that 8 of 23 astrocyte somata from *Ip3r2*$^{-/-}$ mice responded significantly to endothelin, with the response increasing from 7.1 ± 1.9 to 74.7 ± 22.3 dF/F.s ($P = 0.0162$, paired Student's *t* test; **Fig. 4c**).

Next, we examined endothelin-evoked Ca^{2+} fluctuations in astrocyte processes from WT

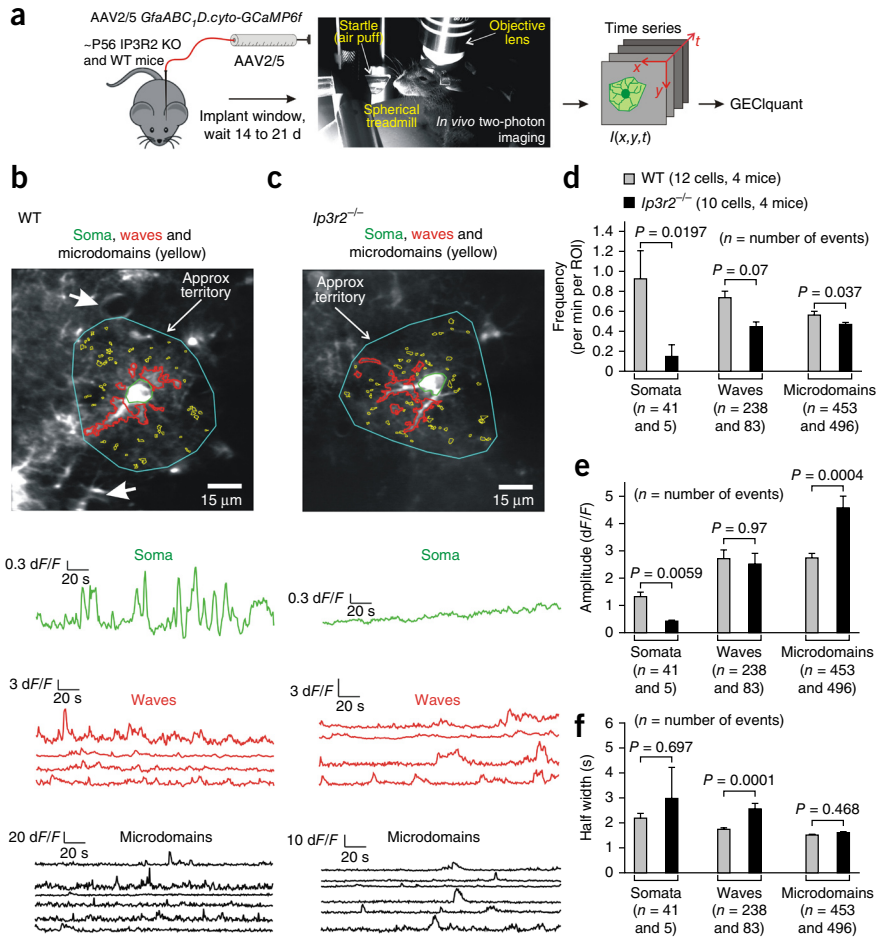

Figure 5 Abundant Ca^{2+} fluctuations persist in astrocyte processes from WT and *Ip3r2*$^{-/-}$ mice *in vivo*. (**a**) Schematic illustrating the experimental approach for *in vivo* imaging in fully awake mice free to rest or run on a spherical treadmill (with no anesthesia). (**b**) Representative images and traces for Ca^{2+} fluctuations measured in a cortical astrocyte from a WT mouse. Three predominant types of Ca^{2+} events are shown: somatic, waves and microdomains. Approximate territory boundaries are outlined in blue, but were not used for data analyses and are shown only for illustrative purposes. (**c**) Data are presented as in **b**, but for an astrocyte from an *Ip3r2*$^{-/-}$ mouse. Representative movies are **Supplementary Videos 5** and **6**. (**d**–**f**) Average data for astrocyte Ca^{2+} fluctuation properties from WT and *Ip3r2*$^{-/-}$ mice during *in vivo* imaging ($n = 12$ astrocytes and 4 mice for each). As stated in the figure, the *n* numbers refer to the numbers of Ca^{2+} fluctuations for each bar, which were averaged for frequency, amplitude and half-width across all cells in **d**–**f**. The data are shown as mean ± s.e.m.

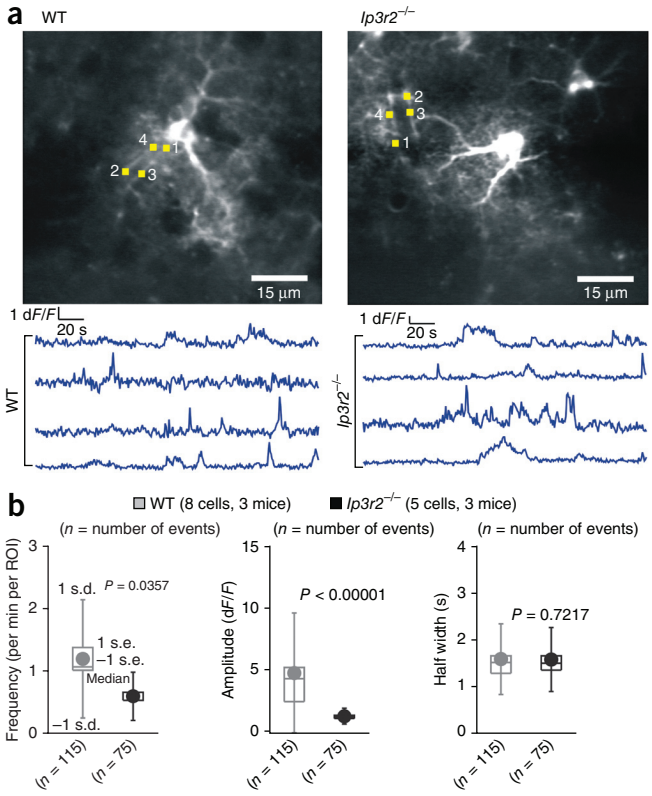

Figure 6 Ca^{2+} fluctuations persist *in vivo* within end feet of cortical astrocytes from *Ip3r2*$^{-/-}$ mice. (**a**) Representative traces and images for Ca^{2+} fluctuations measured in astrocyte end feet from WT and *Ip3r2*$^{-/-}$ mice. (**b**) Average data for astrocyte Ca^{2+} fluctuation properties from WT and *Ip3r2*$^{-/-}$ mice during *in vivo* imaging (WT, $n = 7$ astrocytes and 3 mice; *Ip3r2*$^{-/-}$, $n = 5$ astrocytes and 3 mice). The averages are across all cells and are shown as box and whisker plots.

and *Ip3r2*$^{-/-}$ mice (**Fig. 4d–f**) and measured significant Ca^{2+} elevations in the same proportion of cells from WT and *Ip3r2*$^{-/-}$ mice (~50%, $P < 0.05$, paired Student's *t* test; **Fig. 4d–f**). This shows that *Ip3r2*$^{-/-}$ mice retain GPCR-mediated Ca^{2+} signaling in astrocyte processes that is indiscernible from WT mice. Thus, our data do not support past work suggesting that GPCR-mediated Ca^{2+} signaling is completely abolished in *Ip3r2*$^{-/-}$ mice[10]. Furthermore, given that astrocytes interact with neurons via processes, and because endothelin responses were observed in processes and not in the somata of *Ip3r2*$^{-/-}$ mice, our data support the idea[24,38] that astrocyte somata cannot be used as a proxy measure of Ca^{2+} signaling in processes (**Fig. 4**).

Spontaneous Ca^{2+} fluctuations in cortical astrocytes *in vivo* from WT and *Ip3r2*$^{-/-}$ mice

We considered it important to assess astrocyte Ca^{2+} signaling *in vivo* to be sure that our observations with hippocampal slices were representative of signaling in intact brain. Recent studies have shown that cortical astrocyte somata display ongoing spontaneous Ca^{2+} fluctuations and respond with increased Ca^{2+} fluctuations during *in vivo* startle responses[29,30]. We used this experimental procedure for our evaluations. We microinjected AAV2/5 *GfaABC$_1$D*-GCaMP6f virus into the visual cortex of adult mice, implanted glass cranial windows and then, after 2–3 weeks of recovery, used two-photon microscopy to assess cortical astrocytes in fully awake, non-anesthetized, head-fixed mice that were free to run or rest on a spherical treadmill (**Fig. 5a**).

We first focused on detailed analyses of somata and processes. We assessed spontaneous Ca^{2+} fluctuations in astrocytes in the visual cortex of four WT and four *Ip3r2*$^{-/-}$ mice (during stationary periods when the mice were not in locomotion[29]). We observed spontaneous somatic fluctuations as well as waves and microdomains in processes (**Supplementary Videos 5** and **6**), with properties that largely resembled those observed in hippocampal slices (**Figs. 1** and **2**). Compared with WT mice, *Ip3r2*$^{-/-}$ mice displayed markedly fewer Ca^{2+} fluctuations in the somata, and these fluctuations were reduced in frequency and amplitude relative to WT, although their durations were not substantially different (compared with unpaired Mann-Whitney tests; **Fig. 5d–f**). In contrast with somatic Ca^{2+} fluctuations, waves and microdomains in processes were not markedly affected. We observed only ~5% and ~40% decreases in the frequency of microdomains and waves, respectively, and no decreases in their amplitude or duration (**Fig. 5d–f**). In fact, the amplitudes of microdomain Ca^{2+} fluctuations were significantly increased compared with those of WT mice (**Fig. 5e**). Hence, overall Ca^{2+} fluctuations were reduced largely in the somata of cortical astrocytes and were largely spared in astrocyte processes (**Fig. 5**). This result is apparent from **Supplementary Videos 5** and **6**, from the representative traces of Ca^{2+} fluctuations (**Fig. 5b,c**) and from the average data with statistical comparisons between WT and *Ip3r2*$^{-/-}$ mice (**Fig. 5d–f**). Moreover, the type and subcellular pattern of Ca^{2+} fluctuations in astrocytes was similar between hippocampal astrocytes *in vitro* and cortical astrocytes *in vivo* for both WT and *Ip3r2*$^{-/-}$ mice. This suggests that the Ca^{2+} fluctuations were not a result of the method employed to study them.

Recent studies have shown no measurable alterations in neurovascular coupling in *Ip3r2*$^{-/-}$ mice[14,16,17]. Based on the assumption that all Ca^{2+} fluctuations were abolished in *Ip3r2*$^{-/-}$ mice, these authors concluded that astrocyte Ca^{2+} fluctuations do not contribute to blood vessel function (but see ref. 38). In light of these data, we also analyzed Ca^{2+} fluctuations in astrocyte end feet from the *in vivo* data set. We found numerous Ca^{2+} fluctuations in end feet from WT and *Ip3r2*$^{-/-}$ mice (**Fig. 6a**). Overall, when compared with WT mice, end feet Ca^{2+} fluctuations in *Ip3r2*$^{-/-}$ mice displayed substantial reductions in the frequency and amplitude in individual end feet, but showed no change in duration (**Fig. 6a**). Thus, overall end feet Ca^{2+} fluctuations are halved in number and reduced by ~70% in amplitude, but clearly not abolished (**Fig. 6b**).

Startle-evoked Ca^{2+} fluctuations in cortical astrocytes from WT and *Ip3r2*$^{-/-}$ mice

Startle-evoked Ca^{2+} fluctuations that cover all astrocytes in an imaging field of view are mediated by endogenous norepinephrine release from noradrenergic fibers emanating from the locus coeruleus and acting on astrocyte α_1 adrenoceptors[29,30]. We refer to these as global Ca^{2+} fluctuations to discriminate the terminology from that used for the subcellular Ca^{2+} fluctuations referred to above. We next tested whether cortical astrocytes of non-anesthetized awake behaving mice responded to startle, which was elicited by a gentle puff of air to the face (**Supplementary Video 7**). WT and *Ip3r2*$^{-/-}$ mice were exposed to a brief (3 s) air puff to the face and Ca^{2+} fluctuations were recorded in GCaMP6f-expressing cortical astrocytes using two-photon microscopy (**Fig. 7a**). We readily observed startle-evoked increases in global Ca^{2+} fluctuations in astrocytes from WT mice, which were associated with an increase in the locomotion of the mouse on the spherical treadmill ($n = 4$ mice of each genotype; **Fig. 7**). Such startle-evoked global Ca^{2+} fluctuations encompassed essentially all of the astrocytes in the field of view[29] (**Fig. 7a**). For these analyses, we evaluated astrocyte somatic and process compartments separately

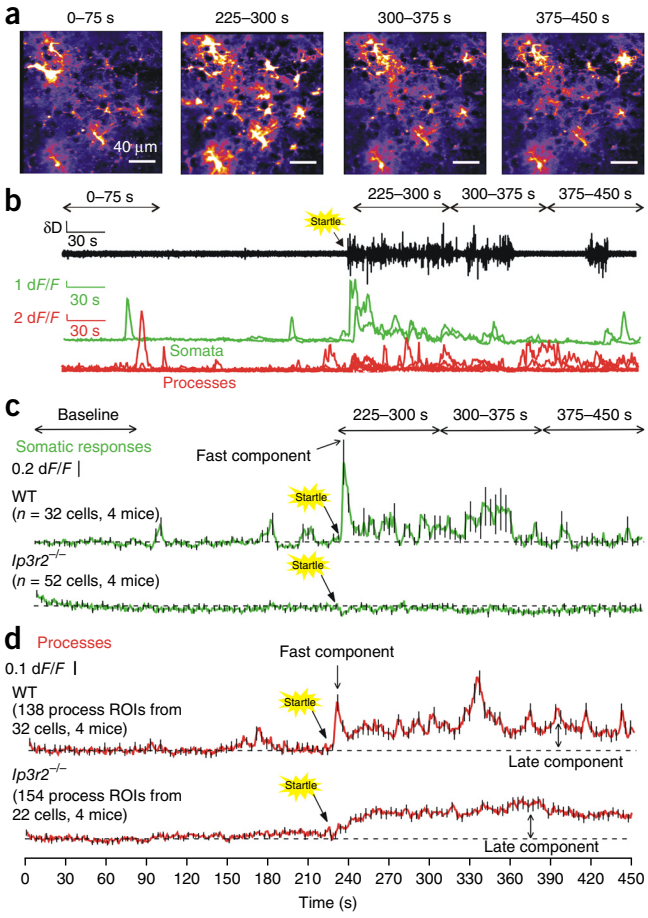

Figure 7 Endogenously evoked astrocyte process Ca^{2+} fluctuations recorded during *in vivo* startle responses reveal early and late components. (**a**) Representative images of Ca^{2+} fluctuations from cortical astrocytes before, during and after startle responses, which were evoked by a puff of air to the face of the mouse (Online Methods and **Supplementary Video 9**). The times written above each of the images correspond to the times shown in the traces in **b** and **c**. Startle was evoked at 225 s. Representative data for WT and *Ip3r2*$^{-/-}$ are shown in **Supplementary Videos 7** and **8**. (**b**) Representative traces for the animal's locomotion on the spherical treadmill along with Ca^{2+} responses of cortical astrocytes for somatic and process fluctuations for the cells shown in **a**. Note that startle-triggered running of the mouse on the ball, as well as Ca^{2+} fluctuations in cortical astrocytes. (**c**) Average data for experiments such as those in **b** for 32 cells from four WT and 52 cells from four *Ip3r2*$^{-/-}$ mice. (**d**) Data are presented as in **c**, but for astrocyte process fluctuations. Note that the responses in the territory displayed a fast/early component and a slow/late component that persisted during these recordings. In the interests of clarity, error bars in **c** and **d** are shown for every fifth data point, but the underlying average traces are for all cells. The data are shown as mean ± s.e.m.

before, during and after startle responses. The somata were easy to identify and process ROIs were chosen to be within ~40 µm of the cell body. However, because all astrocytes in the field of view responded to startle, it was not possible to approximately demarcate whole astrocytes similar to what we did for the hippocampal slice experiments in **Figure 2c**. Thus, for the *in vivo* experiments, we were unable to assess Ca^{2+} fluctuations in whole astrocytes (that is, territories) and restrict our analyses to ROIs in somata and processes.

Startle-evoked global Ca^{2+} fluctuations in cortical astrocytes are reported in **Supplementary Video 8**. These data are presented as still frames before (0–75 s), immediately during (225–300 s) and at two subsequent time periods after the startle (300–375 and 375–450 s) in **Figure 7a**. The exemplar traces in **Figure 7b** show locomotion activity on the spherical treadmill along with representative traces for astrocyte somatic and process Ca^{2+} fluctuations. In the case of somata, fast Ca^{2+} fluctuations were observed ~3 s after startle, which recalls past work[29]. These fluctuations decreased over time in the representative traces and lasted, on average, ~14 ± 1 s (**Fig. 7a–c**). In relation to this, the startle-evoked increase in locomotion lasted 20 ± 10 s (n = 4 mice, range of 3–70 s). Startle-evoked somatic Ca^{2+} fluctuations were completely abolished in *Ip3r2*$^{-/-}$ mice (**Fig. 7c**), but the startle-evoked locomotion lasted 13 ± 4 s (n = 4 mice).

In contrast with somatic fluctuations, the Ca^{2+} fluctuations measured in astrocyte processes in response to startle were multiphasic. Soon after startle, the response comprised a fast component that displayed a similar time course to the somatic response (that is, it peaked in ~3 s and lasted 13 ± 4 s). However, in processes, this fast component was followed by a delayed response (late component) that leveled off at ~50 s after the startle and was maintained for the duration of the recording and returned back to baseline slowly over 5–10 min, that is, with a time course far in excess of the startle-evoked locomotion of 20 ± 10–s duration. The late component of the process responses could be easily seen in the representative traces and in the average data (**Fig. 7b–d**). The differences in time course of the fast and late components of the process response (**Fig. 7d**), as well as the lack of the late component in the somata (**Fig. 7c**), suggests that the two components may be mediated by distinct mechanisms. Consistent with this, the fast component of the process response was abolished in *Ip3r2*$^{-/-}$ mice (**Fig. 7d**). In contrast, the late component was completely unaffected in *Ip3r2*$^{-/-}$ mice (**Fig. 7d**).

Supplementary Figure 11 summarizes average differences and statistical comparisons (using paired Mann-Whitney tests) between WT and *Ip3r2*$^{-/-}$ mice at three time periods relative to baseline for startle responses. Overall, the somatic response was almost completely abolished (**Supplementary Fig. 11a**), whereas the startle-evoked response in processes was not affected at the time points examined (**Supplementary Fig. 11b**). These data provide compelling evidence that astrocyte physiological Ca^{2+} fluctuations persist *in vivo* in *Ip3r2*$^{-/-}$ mice.

Prazosin did not inhibit startle-evoked astrocyte process Ca^{2+} fluctuations in WT or *Ip3r2*$^{-/-}$ mice

We assessed the effect of the α1-adrenoceptor antagonist prazosin on startle-evoked Ca^{2+} fluctuations in WT and *Ip3r2*$^{-/-}$ mice (**Fig. 8**). Cranial window–implanted WT and *Ip3r2*$^{-/-}$ mice expressing GCaMP6f in astrocytes were subjected to a 3-s air puff to the face, and baseline startle responses were recorded from cortical astrocytes (n = 4 mice of each genotype). These mice were then injected with prazosin (1 mg per kg of body weight, intraperitoneal) and 30 min later, startle responses were recorded in the same field of view of astrocytes to allow direct comparison of control versus prazosin effects in the same cells (**Fig. 8a**). Prazosin completely inhibited startle-induced Ca^{2+} fluctuations in astrocyte somata of WT mice (**Fig. 8b**), but, as expected, did not alter the lack of Ca^{2+} fluctuations observed from the somata of *Ip3r2*$^{-/-}$ mice (**Fig. 8c**). In the processes of WT astrocytes, prazosin selectively inhibited the fast component of the startle-evoked Ca^{2+} event and had no effect on the late component (**Fig. 8d**). Similarly in the *Ip3r2*$^{-/-}$ mice, we measured no significant effect of prazosin on the astrocyte process Ca^{2+} fluctuations or on the late component following startle (**Fig. 8e**). Taken together, our *in vivo* evaluations show

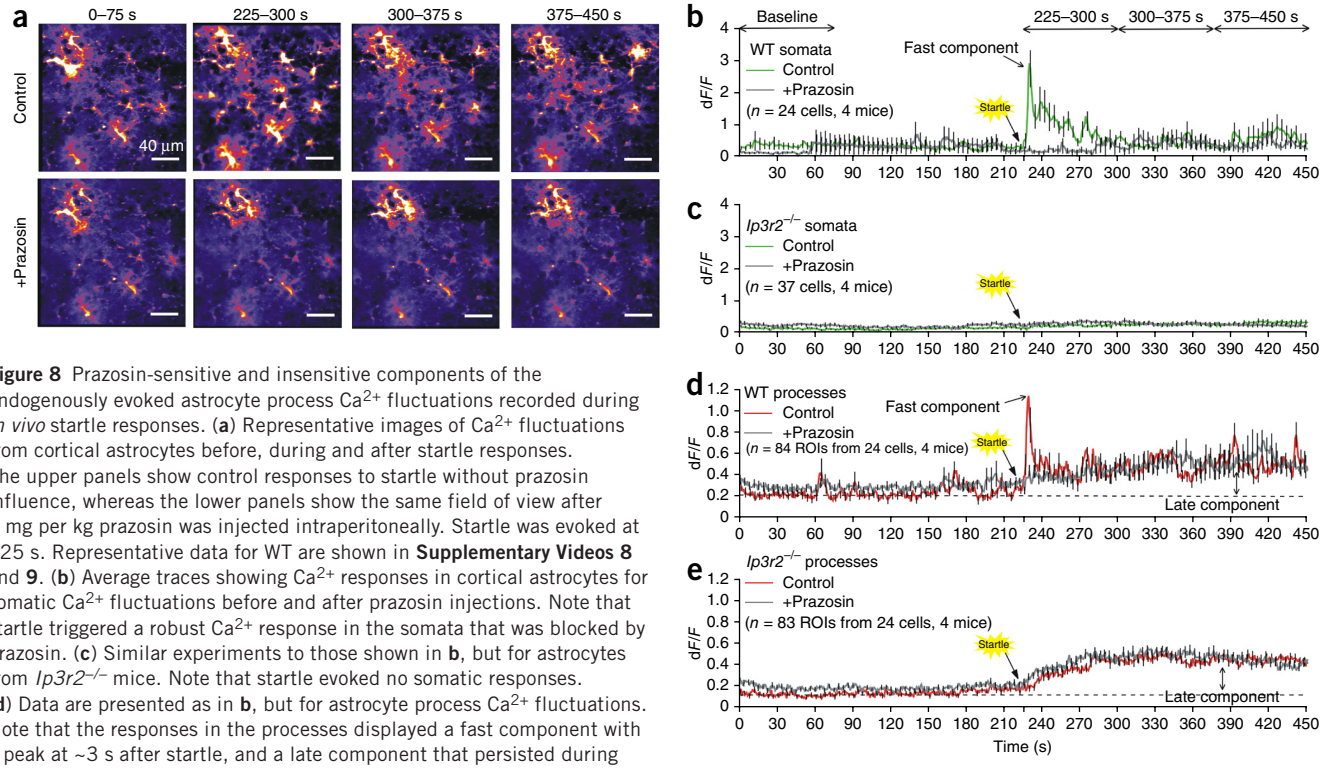

Figure 8 Prazosin-sensitive and insensitive components of the endogenously evoked astrocyte process Ca^{2+} fluctuations recorded during *in vivo* startle responses. (**a**) Representative images of Ca^{2+} fluctuations from cortical astrocytes before, during and after startle responses. The upper panels show control responses to startle without prazosin influence, whereas the lower panels show the same field of view after 1 mg per kg prazosin was injected intraperitoneally. Startle was evoked at 225 s. Representative data for WT are shown in **Supplementary Videos 8** and **9**. (**b**) Average traces showing Ca^{2+} responses in cortical astrocytes for somatic Ca^{2+} fluctuations before and after prazosin injections. Note that startle triggered a robust Ca^{2+} response in the somata that was blocked by prazosin. (**c**) Similar experiments to those shown in **b**, but for astrocytes from *Ip3r2*$^{-/-}$ mice. Note that startle evoked no somatic responses. (**d**) Data are presented as in **b**, but for astrocyte process Ca^{2+} fluctuations. Note that the responses in the processes displayed a fast component with a peak at ~3 s after startle, and a late component that persisted during these recordings. Prazosin blocked only the fast component. (**e**) Data are presented as in **d**, but for *Ip3r2*$^{-/-}$ mice. The slow component of the Ca^{2+} response triggered by startle was present in the *Ip3r2*$^{-/-}$ mice and was insensitive to prazosin. The results shown in this figure are from four WT and four *Ip3r2*$^{-/-}$ mice. In the interests of clarity, error bars in **b**–**e** are shown for every fifth data point, but the underlying average traces are for all cells. The data are shown as mean ± s.e.m.

that a previously unknown late component of the Ca^{2+} fluctuations measured in cortical astrocytes after startle persist in *Ip3r2*$^{-/-}$ mice and are not mediated by α_1-adrenoceptors or by IP3R2 receptors.

DISCUSSION

We used state-of-the art methods to image and analyze astrocyte Ca^{2+} fluctuations with GCaMP6f in astrocytes in brain slices and *in vivo*. There are four main findings from the work. First, in WT mice, the majority of Ca^{2+} fluctuations occurred in astrocyte processes and not in the somata. Second, Ca^{2+} fluctuations were not abolished in any astrocyte compartment and were not markedly altered in astrocyte processes of *Ip3r2*$^{-/-}$ mice. Third, a model GPCR agonist (endothelin) reliably evoked Ca^{2+} fluctuations in the processes of astrocytes from WT and *Ip3r2*$^{-/-}$ mice, although the somatic response was significantly reduced in *Ip3r2*$^{-/-}$ mice. Fourth, startle-evoked Ca^{2+} fluctuations in astrocyte processes *in vivo* consisted of two phases: an early component mediated by α_1-adrenoceptors[29,30] and a late component that was independent of α_1-adrenoceptors and IP3R2-mediated signaling.

As shown in several recent studies[23,24,29,39], genetically encoded calcium indicators (GECIs) are excellent tools for studying astrocyte Ca^{2+} fluctuations and have shed new light on areas of the cells such as processes that have previously been difficult to explore. We used GCaMP6f, which is as fast as organic Ca^{2+} indicator dyes[22], although this speed was not crucial for measuring astrocyte Ca^{2+} fluctuations, which lasted hundreds of milliseconds to seconds[24]. Evaluations have shown that bulk loading is not appropriate for studying the vast majority of an astrocyte's area[32]. We suggest that the previous reliance on bulk loading of organic Ca^{2+} indicator dyes has underestimated the true extent of astrocyte Ca^{2+} signaling and missed the vast majority of fluctuations that occur in processes. This view is supported by recent studies in which main astrocyte processes[32,38,40,41] and entire astrocytes[23,24] have been examined. Data gathered with organic Ca^{2+} indicator dyes has led to the erroneous conclusion that all spontaneous and GPCR-mediated Ca^{2+} signaling is abolished in hippocampal astrocytes in *Ip3r2*$^{-/-}$ mice[9–11]. Because of this finding, subsequent studies have suggested that astrocyte Ca^{2+} fluctuations have no detectable role in neural functions, even though these conclusions are at odds with data using different approaches[3,7,8]. However, we found that measuring Ca^{2+} fluctuations in physiological astrocyte compartments is necessary to understand how astrocytes contribute to brain function, an aspect not addressed previously. This is analogous to the need to understand signaling in dendritic spines and nerve terminals, which are distal compartmentalized subcellular structures akin to astrocyte processes.

Our evaluations revealed that the overall pattern of Ca^{2+} fluctuations within astrocytes was similar between hippocampal astrocytes in brain slices and cortical astrocytes *in vivo* for WT and *IP3R2*$^{-/-}$ mice, implying that the measured Ca^{2+} fluctuations were not the consequence of the method employed to study them. Moreover, wave and microdomain Ca^{2+} fluctuations similar to those observed in *IP3R2*$^{-/-}$ mice could also be seen in WT mice after intracellular store depletion. Additionally, a significant proportion of wave and microdomain Ca^{2+} fluctuations were due to transmembrane Ca^{2+} fluxes. Thus, careful analysis of WT and *Ip3r2*$^{-/-}$ mice revealed Ca^{2+} fluctuations within astrocyte processes that are IP3R2 independent.

What are the relative contributions of the startle response and locomotion for the observed Ca^{2+} fluctuations? Our data show that the fast component of the Ca^{2+} fluctuations in somata and processes lasted ~14 s and thus displayed a similar duration to locomotion[29], which lasted 13–20 s. However, the late component of the Ca^{2+} fluctuations

lasted far longer (>5 min) than the 13–20-s-long locomotion evoked by startle. Moreover, cortical astrocytes are directly targeted by locus coeruleus projections[29,30,42], but the relatively long (~3 s) latency between startle onset and astrocyte Ca^{2+} fluctuations in processes and somata seems too slow to be causal for the fast tens-of-milliseconds timescale norepinephrine-mediated responses in cortical neurons[43]. It seems likely that astrocyte Ca^{2+} fluctuations may drive slow tens-of-seconds timescale changes in K^+ concentration[44], regulate blood flow[3] via Ca^{2+}-dependent phospholipase A2, control neurotransmitter uptake[45,46] or respond to the release of neuromodulators[8]. We hypothesize that the slow elevations in basal Ca^{2+} in processes may also regulate the tonic release of D-serine[47] and hence set a prolonged time window for NMDA receptor–dependent plasticity to occur in microcircuits that received norepinephrine as a volume transmitter. Consistent with this proposal, resting D-serine levels in cortex are regulated by astrocytes and the availability of D-serine gates synaptic potentiation[48]. In this scenario, astrocytes would function as intermediary neuromodulators, that is, they would bridge diffuse norepinephrine volume transmission and its effects on synapses.

More generally, exploration of the signaling potential and downstream effects of astrocyte Ca^{2+} fluctuations requires the development of new methods to abolish all of the types of Ca^{2+} fluctuations that we have described. As recently discussed[5], when this new method is available and rigorously validated, it may then be opportune to determine the effects of total loss of astrocyte Ca^{2+} fluctuations on blood vessels, neurons and mouse behavior. From these perspectives, rigorous biophysical models and further experiments are necessary to explore astrocyte Ca^{2+} signaling and to identify the sources of the previously unknown Ca^{2+} fluctuations that we report, which include intracellular release and extracellular entry.

We conclude that the paucity of data on processes that comprise entire astrocytes has contributed to the current controversies in the field on the relevance of Ca^{2+} signaling. Our findings call for a necessary degree of caution when interpreting past studies that concluded astrocyte Ca^{2+} fluctuations had no role in neuronal and blood vessel function[9,10,14–16], as those studies relied on the assumption that all Ca^{2+} signaling was abolished in *Ip3r2*$^{-/-}$ mice[9–11]. Our data, gathered in brain slices and *in vivo,* invalidate this view and reveal a previously unknown form of astrocyte signaling that is independent of both IP3R2 and α_1-adrenoceptors and is found in astrocyte processes.

METHODS

Methods and any associated references are available in the online version of the paper.

Note: Any Supplementary Information and Source Data files are available in the online version of the paper.

ACKNOWLEDGMENTS

The authors are grateful to current and past members of the laboratories for discussions and comments. Thanks also to M.V. Sofroniew for sharing equipment and to J. Chen for sharing mice. Special thanks to M.D. Haustein who helped with the initial testing of GECIquant and made valuable suggestions on its development. We thank C. Octeau for comments on the paper. Most of the work was supported by the US National Institutes of Health (NIH, NS060677). B.S.K., R.S. and S.V. were also supported by NIH grants (MH099559A, MH104069) and the CHDI Foundation. P.G. and B.S.H. were supported by NIH MH101198-1 and a Simon's Foundation Circuits Grant.

AUTHOR CONTRIBUTIONS

R.S. carried out the molecular biology, hippocampal stereotaxic injections and most of the slice experiments with help from A.D.J. and H.C. B.S.H. performed all of the cortical virus injections and cranial window implantations for the *in vivo* experiments. B.S.H. and R.S. did the *in vivo* imaging together. S.V. wrote the GECIquant software and R.S. tested it. P.G. shared expertise on *in vivo* calcium imaging. H.Z. made and shared GCaMP6f knock-in mice. R.S. and B.S.K. analyzed data. B.S.K. directed the experiments, assembled the figures and wrote the paper. All of the authors contributed to the final version.

COMPETING FINANCIAL INTERESTS

The authors declare no competing financial interests.

1. Bushong, E.A., Martone, M.E., Jones, Y.Z. & Ellisman, M.H. Protoplasmic astrocytes in CA1 stratum radiatum occupy separate anatomical domains. *J. Neurosci.* **22**, 183–192 (2002).
2. Wilhelmsson, U. *et al.* Redefining the concept of reactive astrocytes as cells that remain within their unique domains upon reaction to injury. *Proc. Natl. Acad. Sci. USA* **103**, 17513–17518 (2006).
3. Attwell, D. *et al.* Glial and neuronal control of brain blood flow. *Nature* **468**, 232–243 (2010).
4. Barres, B.A. The mystery and magic of glia: a perspective on their roles in health and disease. *Neuron* **60**, 430–440 (2008).
5. Khakh, B.S. & McCarthy, K.D. Astrocyte calcium signals: from observations to functions and the challenges therein. *Cold Spring Harb. Perspect. Biol.* published online, doi:10.1101/cshperspect.a020404 (20 Jan 2015).
6. Cornell-Bell, A.H., Finkbeiner, S.M., Cooper, M.S. & Smith, S.J. Glutamate induces calcium waves in cultured astrocytes: long-range glial signaling. *Science* **247**, 470–473 (1990).
7. Allen, N.J. Astrocyte regulation of synaptic behavior. *Annu. Rev. Cell Dev. Biol.* **30**, 439–463 (2014).
8. Halassa, M.M. & Haydon, P.G. Integrated brain circuits: astrocytic networks modulate neuronal activity and behavior. *Annu. Rev. Physiol.* **72**, 335–355 (2010).
9. Petravicz, J., Fiacco, T.A. & McCarthy, K.D. Loss of IP3 receptor-dependent Ca^{2+} increases in hippocampal astrocytes does not affect baseline CA1 pyramidal neuron synaptic activity. *J. Neurosci.* **28**, 4967–4973 (2008).
10. Agulhon, C., Fiacco, T.A. & McCarthy, K.D. Hippocampal short- and long-term plasticity are not modulated by astrocyte Ca^{2+} signaling. *Science* **327**, 1250–1254 (2010).
11. Agulhon, C. *et al.* Modulation of the autonomic nervous system and behaviour by acute glial cell Gq protein-coupled receptor activation *in vivo*. *J. Physiol.* (*Lond.*) **591**, 5599–5609 (2013).
12. Zhang, Y. *et al.* An RNA-Sequencing transcriptome and splicing database of glia, neurons, and vascular cells of the cerebral cortex. *J. Neurosci.* **34**, 11929–11947 (2014).
13. Petravicz, J., Boyt, K.M. & McCarthy, K.D. Astrocyte IP3R2-dependent Ca(2+) signaling is not a major modulator of neuronal pathways governing behavior. *Front. Behav. Neurosci.* **8**, 384 (2014).
14. Nizar, K. *et al. In vivo* stimulus-induced vasodilation occurs without IP3 receptor activation and may precede astrocytic calcium increase. *J. Neurosci.* **33**, 8411–8422 (2013).
15. Takata, N. *et al.* Cerebral blood flow modulation by Basal forebrain or whisker stimulation can occur independently of large cytosolic Ca^{2+} signaling in astrocytes. *PLoS ONE* **8**, e66525 (2013).
16. Bonder, D.E. & McCarthy, K.D. Astrocytic Gq-GPCR-linked IP3R-dependent Ca^{2+} signaling does not mediate neurovascular coupling in mouse visual cortex *in vivo*. *J. Neurosci.* **34**, 13139–13150 (2014).
17. Takata, N. *et al.* Astrocyte calcium signaling transforms cholinergic modulation to cortical plasticity *in vivo*. *J. Neurosci.* **31**, 18155–18165 (2011).
18. Chen, N. *et al.* Nucleus basalis–enabled stimulus-specific plasticity in the visual cortex is mediated by astrocytes. *Proc. Natl. Acad. Sci. USA* **109**, E2832–E2841 (2012).
19. Navarrete, M. *et al.* Astrocytes mediate *in vivo* cholinergic-induced synaptic plasticity. *PLoS Biol.* **10**, e1001259 (2012).
20. Perez-Alvarez, A., Navarrete, M., Covelo, A., Martín, E.D. & Araque, A. Structural and functional plasticity of astrocyte processes and dendritic spine interactions. *J. Neurosci.* **34**, 12738–12744 (2014).
21. Wang, F. *et al.* Astrocytes modulate neural network activity by Ca^{2+}-dependent uptake of extracellular K+. *Sci. Signal.* **5**, ra26 (2012).
22. Chen, T.W. *et al.* Ultrasensitive fluorescent proteins for imaging neuronal activity. *Nature* **499**, 295–300 (2013).
23. Shigetomi, E. *et al.* Imaging calcium microdomains within entire astrocyte territories and end feet with GCaMPs expressed using adeno-associated viruses. *J. Gen. Physiol.* **141**, 633–647 (2013).
24. Haustein, M.D. *et al.* Conditions and constraints for astrocyte calcium signaling in the hippocampal mossy fiber pathway. *Neuron* **82**, 413–429 (2014).
25. Jiang, R., Haustein, M.D., Sofroniew, M.V. & Khakh, B.S. Imaging intracellular Ca^{2+} signals in striatal astrocytes from adult mice using genetically-encoded calcium indicators. *J. Vis. Exp.* published online, doi:10.3791/51972 (19 November 2014).
26. Sun, W. *et al.* Glutamate-dependent neuroglial calcium signaling differs between young and adult brain. *Science* **339**, 197–200 (2013).
27. Nimmerjahn, A., Mukamel, E.A. & Schnitzer, M.J. Motor behavior activates Bergmann glial networks. *Neuron* **62**, 400–412 (2009).
28. Thrane, A.S. *et al.* General anesthesia selectively disrupts astrocyte calcium signaling in the awake mouse cortex. *Proc. Natl. Acad. Sci. USA* **109**, 18974–18979 (2012).

29. Paukert, M. *et al.* Norepinephrine controls astroglial responsiveness to local circuit activity. *Neuron* **82**, 1263–1270 (2014).
30. Ding, F. *et al.* α1-Adrenergic receptors mediate coordinated Ca(2+) signaling of cortical astrocytes in awake, behaving mice. *Cell Calcium* **54**, 387–394 (2013).
31. Fiacco, T.A. *et al.* Selective stimulation of astrocyte calcium in situ does not affect neuronal excitatory synaptic activity. *Neuron* **54**, 611–626 (2007).
32. Reeves, A.M., Shigetomi, E. & Khakh, B.S. Bulk loading of calcium indicator dyes to study astrocyte physiology: key limitations and improvements using morphological maps. *J. Neurosci.* **31**, 9353–9358 (2011).
33. Fiacco, T.A., Agulhon, C. & McCarthy, K.D. Sorting out astrocyte physiology from pharmacology. *Annu. Rev. Pharmacol. Toxicol.* **49**, 151–174 (2009).
34. Shigetomi, E., Bowser, D.N., Sofroniew, M.V. & Khakh, B.S. Two forms of astrocyte calcium excitability have distinct effects on NMDA receptor-mediated slow inward currents in pyramidal neurons. *J. Neurosci.* **28**, 6659–6663 (2008).
35. Anders, S. *et al.* Spatial properties of astrocyte gap junction coupling in the rat hippocampus. *Philos. Trans. R Soc. Lond. B Biol. Sci.* **369**, 20130600 (2014).
36. Wallraff, A. *et al.* The impact of astrocytic gap junctional coupling on potassium buffering in the hippocampus. *J. Neurosci.* **26**, 5438–5447 (2006).
37. Nett, W.J., Oloff, S.H. & McCarthy, K.D. Hippocampal astrocytes in situ exhibit calcium oscillations that occur independent of neuronal activity. *J. Neurophysiol.* **87**, 528–537 (2002).
38. Otsu, Y. *et al.* Calcium dynamics in astrocyte processes during neurovascular coupling. *Nat. Neurosci.* **18**, 210–218 (2015).
39. Shigetomi, E., Kracun, S., Sofroniew, M.V. & Khakh, B.S. A genetically targeted optical sensor to monitor calcium signals in astrocyte processes. *Nat. Neurosci.* **13**, 759–766 (2010).
40. Panatier, A. *et al.* Astrocytes are endogenous regulators of basal transmission at central synapses. *Cell* **146**, 785–798 (2011).
41. Di Castro, M.A. *et al.* Local Ca^{2+} detection and modulation of synaptic release by astrocytes. *Nat. Neurosci.* **14**, 1276–1284 (2011).
42. Bekar, L.K., He, W. & Nedergaard, M. Locus coeruleus alpha-adrenergic-mediated activation of cortical astrocytes *in vivo*. *Cereb. Cortex* **18**, 2789–2795 (2008).
43. Polack, P.O., Friedman, J. & Golshani, P. Cellular mechanisms of brain state–dependent gain modulation in visual cortex. *Nat. Neurosci.* **16**, 1331–1339 (2013).
44. Wang, F., Xu, Q., Wang, W., Takano, T. & Nedergaard, M. Bergmann glia modulate cerebellar Purkinje cell bistability via Ca^{2+}-dependent K^+ uptake. *Proc. Natl. Acad. Sci. USA* **109**, 7911–7916 (2012).
45. Shigetomi, E., Tong, X., Kwan, K.Y., Corey, D.P. & Khakh, B.S. TRPA1 channels regulate astrocyte resting calcium and inhibitory synapse efficacy through GAT-3. *Nat. Neurosci.* **15**, 70–80 (2012).
46. Muthukumar, A.K., Stork, T. & Freeman, M.R. Activity-dependent regulation of astrocyte GAT levels during synaptogenesis. *Nat. Neurosci.* **17**, 1340–1350 (2014).
47. Shigetomi, E., Jackson-Weaver, O., Huckstepp, R.T., O'Dell, T.J. & Khakh, B.S. TRPA1 channels are regulators of astrocyte basal calcium levels and long-term potentiation via constitutive D-serine release. *J. Neurosci.* **33**, 10143–10153 (2013).
48. Fossat, P. *et al.* Glial D-serine gates NMDA receptors at excitatory synapses in prefrontal cortex. *Cereb. Cortex* **22**, 595–606 (2012).

ONLINE METHODS

All experimental procedures were approved by the University of California Los Angeles Office for Protection of Research Subjects and the Chancellor's Animal Research Committee. All the mice were housed on a 12-h light dark cycle with no more than five mice per cage. All of the experiments were done between 9 a.m. and 9 p.m.

Mice, molecular biology and adeno-associated virus. *Ip3r2*$^{-/+}$ mice were obtained from J. Chen (University of California at San Diego) and maintained as a heterozygous line. Homozygotes and WT littermates were used for experiments when they reached age postnatal day 46–67 (P46–P67). To generate AAV2/5 capable of expressing GCaMP6f in astrocytes, we modified plasmid pZac2.1final (Penn Vector Core), as reported in detail in previous work[23]. Briefly, we removed the CMV promoter flanked by BglII and HindIII sites and replaced it with the minimal (~700 bp) *GfaABC$_1$D* astrocyte-specific promoter, which was amplified by PCR from Addgene plasmid #19974. We then cloned *GCaMP6f* into this modified pZac2.1 vector between EcoRI and *XbaI* sites to generate plasmids we called pZac2.1 *GfaABC$_1$D GCaMP6f*. The fully sequenced pZac2.1 plasmids were sent to the Penn Vector Core, which used them to generate AAV2/5 for each construct at a concentration of ~2×10^{13} genome copies per ml (gc ml^{-1}). All our virus constructs have been deposited at Addgene in the Khakh laboratory repository for unrestricted distribution (http://www.addgene.org/Baljit_Khakh). The plasmid for pZac2.1 *GfaABC$_1$D GCaMP6f* has an Addgene ID number of 52925. The AAV is also available for purchase from the UPenn Vector Core.

One specific experiment (**Supplementary Fig. 8**) used GCaMP6f^{flx} mice (JAX #024105) that were crossed with GLAST-Cre/ERT2 mice (JAX #012586), as described previously for GCaMP3^{flx} mice[29]. The GCaMP6f^{flx} mice were donated to JAX[49] by H. Zeng (Allen Institute for Brain Sciences). All of the information on the generation and genotyping of both lines is available at JAX by searching online for the mouse identification numbers, 024105 and 012586. Once double transgenic mice were 2 months of age, they were administered 100 µl tamoxifen at 75 mg per kg of body weight once a day for 5 d by intraperitoneal injection. 2 weeks after the last injection, the mice were used to harvest brain slices exactly as described above.

Surgery and *in vivo* microinjections for hippocampal astrocyte imaging *in situ*. Postnatal day 46–67 (P46–P67) male and female *Ip3r2*$^{-/-}$ and WT littermate mice were used. All surgical procedures were conducted under general anesthesia using continuous isoflurane (induction at 5%, maintenance at 1–2.5%, vol/vol). Depth of anesthesia was monitored continuously and adjusted when necessary. After induction of anesthesia, the mice were fitted into a stereotaxic frame, with their heads secured by blunt ear bars and their noses placed into an anesthesia and ventilation system (David Kopf Instruments). Mice were administered 0.05 ml of buprenorphine (0.1 mg ml^{-1}; Buprenex) subcutaneously before surgery. The surgical incision site was then cleaned three times with 10% povidone iodine and 70% ethanol. Skin incisions were made, followed by craniotomies of 2–3 mm in diameter above the left parietal cortex using a small steel burr (Fine Science Tools) powered by a high speed drill (K.1070; Foredom). Saline (0.9%) was applied onto the skull to reduce heating caused by drilling. Unilateral viral injections were performed by using stereotaxic apparatus (David Kopf Instruments) to guide the placement of beveled glass pipettes (World Precision Instruments) into the left hippocampus (2 mm posterior to bregma, 1.5 mm lateral to midline, and 1.6 mm from the pial surface). 1.5 µl AAV2/5 *GfaABC$_1$D GCaMP6f* (at 2.4×10^{13} gc ml^{-1}) was injected using a syringe pump (Pump11 PicoPlus Elite, Harvard Apparatus). Glass pipettes were left in place for at least 10 min. Surgical wounds were closed with single external 5–0 nylon sutures. After surgery, animals were allowed to recover overnight in cages placed partially on a low voltage heating pad. Buprenorphine was administered two times per day for up to 2 d after surgery. In addition, trimethoprim and sulfamethoxazole (40 and 200 mg, respectively, per 500 ml water) were dispensed in the drinking water for 1 week. Mice were killed at 14–21 d after surgery for imaging (typically 14 d). We chose this period because generally it takes ~2 weeks to achieve GECI expression in cells by AAV infection and because of past experiences[23,24,47].

Preparation of brain slices and confocal Ca^{2+} imaging. Coronal slices of hippocampus (300 µm) were cut in solution comprising (mM): 87 NaCl, 25 $NaHCO_3$, 2.5 KCl, 1.25 NaH_2PO_4, 25 D-glucose, 75 sucrose, 7 $MgCl_2$ and 0.5 $CaCl_2$, saturated with 95% O_2 and 5% CO_2. Slices were incubated at ~34 °C for 30 min and subsequently stored at 21–23 °C in artificial cerebrospinal fluid (aCSF) comprising (mM): 126 NaCl, 2.5 KCl, 1.3 $MgCl_2$, 10 D-glucose, 2.4 $CaCl_2$, 1.24 NaH_2PO_4, and 26 $NaHCO_3$, saturated with 95% O_2 and 5% CO_2. All other slice procedures were exactly as described previously[23]. All imaging was performed using commercially available off-the-shelf and standard confocal microscopes. In brief, cells were mostly imaged using a confocal microscope (Fluoview 300; Olympus) with a 40× water-immersion objective lens with a numerical aperture of 0.8, and a few cells were imaged with another confocal microscope (Fluoview 1000; Olympus) using the same lens. We used the 488-nm line of an Argon laser, with the intensity adjusted to 0.5–5% of the maximum output, which was 16.9 mW in the case of the Fluoview 300 and 10 mW in the case of the Fluoview 1000. The emitted light pathway consisted of an emission high pass filter (>510 nm) before the photomultiplier tube. These settings were chosen based on the known properties of GCaMPs[23]. Astrocytes were selected from the CA1 stratum radiatum region and were typically ~40 µm from the slice surface. Endothelin was applied in the bath at ~3 ml min^{-1} using a peristaltic pump. In the case of the CPA experiments, baseline movies without CPA were acquired at 1 frame per s for 5 min. CPA was applied at 20 µM for 30 min, after which a second movie of the same cell was acquired in the presence of CPA at 1 frame per s for 5 min. For the Ca^{2+} free experiments shown in **Figure 3**, the conditions were exactly as described above except that no Ca^{2+} was added to the Ca^{2+} free buffer.

Head-bar installation, virus injection, and cranial window implantation for *in vivo* imaging. Adult (P46–67) male and female *Ip3r2*$^{-/-}$ mice and WT littermates were anesthetized with isoflurane (4% for induction, 1–1.5% vol/vol for maintenance) and placed in a stereotaxic frame (Kopf), with body temperature kept at ~37 °C with a feedback-controlled heating pad (Harvard Apparatus). After removing the scalp and clearing the skull of connective tissues, a custom-made lightweight metal head-bar was fixed onto the skull with cyanoacrylate adhesive (Krazy Glue) and covered with black dental cement (Ortho-Jet). A circular craniotomy (3-mm diameter) was then performed above the primary visual cortex V1 (centered at −2.5 mm lateral from lambda). With the skull opened and the dura intact, the AAV2/5-*GfaABC$_1$D-GCaMP6f* virus was injected at two sites (1.5 µl each) near the center of the craniotomy, at a depth of 150–200 µm. After the injections, a glass cranial window consisting of a 3-mm diameter round #1 coverslip was implanted in the craniotomy, flush with the skull surface, and sealed in place using tissue adhesive (Vetbond). The exposed skull surrounding the cranial window was then completely covered with black dental cement to build a small chamber for imaging with a water-immersion objective. After surgery, animals were returned to their home cages for 2–3 weeks for recovery and viral gene expression before subjecting to imaging experiments. Extreme care was taken to ensure that the dura experienced no damage or major bleeding before and after cranial window implantation. Mice with damaged dura or unclear window were discarded and not used for imaging experiments.

***In vivo* two-photon imaging and mouse movement tracking.** Two-photon laser-scanning microscopy was performed with a moveable objective microscope (Sutter MOM) using a Ti-Sapphire laser (Coherent Ultra II) at 920 nm, through a 40× 0.8 NA water-immersion objective (Olympus). The objective was mounted at a tilt of 30 degrees to the vertical axis in order to image with the light path perpendicular to the cranial window and the cortical surface. Images were acquired using the ScanImage software (Vidrio Technologies)[50] and processed with ImageJ (NIH). Fully awake mice, without any anesthesia, were mounted on top of a spherical treadmill by securing its head-bar onto a custom-made head-bar holder under the microscope. The treadmill consisted of an 8-inch diameter Styrofoam ball resting inside another Styrofoam hollow half-sphere (Graham Sweet Studios) into which a constant stream of compressed air was blown to keep the ball afloat, allowing mice to freely run or rest on top. Images were acquired every 750 ms (1.33 Hz). To track the animals' locomotion, the treadmill motion was measured every 25 ms (40 Hz) by a custom-designed optical sensor whose signals were converted into two servo pulse analog signals (front-back and left-right) using an external PIC microcontroller. The locomotion data were acquired simultaneously with the calcium imaging data and synchronized through the scanning mirror signals. These analog signals were digitized with a NIDAQ board

doi:10.1038/nn.4001

(National Instruments) and acquired with the WinEDR software (Strathclyde). The microscope and treadmill were encased in a light-tight box, and the animals were kept in darkness without visible visual stimuli during the imaging sessions. Before experiments, mice were acclimated to the head fixation and to resting and running on the spherical treadmill, as previously described[43].

***In vivo* startle induction and drug administration.** Startle was induced by presenting a brief air puff to the face of the mice while the mice were resting on top of the spherical treadmill during the imaging sessions. The air puff was delivered by pressing a hand-pump air compressor (28 × 5 cm) attached to a ¼-inch PVC tubing with its opening positioned ~1 cm away from the nostril of the mice (**Fig. 4a**). One press of the hand pump generates a ~3-s-long gentle air puff. Behavioral startle was confirmed by the locomotion induced immediately after presenting the air puff. For the prazosin administration experiments, the mice were positioned on the spherical treadmill and control/baseline images were acquired before prazosin administration. After baseline imaging, the animals were taken off the spherical treadmill and injected with prazosin (1 mg per kg intraperitoneal, Sigma) while fully awake. After injection, these mice were immediately returned to the spherical treadmill and the identical fields of view used for baseline imaging were found, to allow for the direct comparison of prazosin effects in the same population of astrocytes. These mice rested on the treadmill in darkness for ~30 min before imaging commenced again to record post-prazosin Ca^{2+} responses.

Ca^{2+} fluctuation detection using GECIquant and other aspects of data analysis. Detection of astrocyte regions of interest (ROI) containing Ca^{2+} fluctuations was performed in a semi-automated manner using the GECIquant program developed using the open source ImageJ analyses platform. The same procedure was followed for brain slice and *in vivo* data. The GECIquant program is implemented in Java-based ImageJ script language and runs as a plugin on ImageJ. The input to GECIquant is a confocal two-dimensional fluorescence image stack (8 or 16 or 32-bit) of arbitrary frame size, a user defined sampling rate and with time as the third dimension (*t* stack). Data outputs of GECIquant include ROI intensity changes in time, ROI areas and centroid distances of each ROI from a reference ROI. Graphical outputs of GECIquant include ROI intensity kymographs and sub-stacks consisting of fluctuations. **Supplementary Note 1** provides the script and **Supplementary Note 2** provides a user manual for GECIquant.

Having analyzed all the data shown in this study, we observed three distinct types of spontaneous subcellular Ca^{2+} fluctuations within astrocytes, which we describe below and then clarify how they were detected within GECIquant. We classify Ca^{2+} fluctuations as: (1) somatic fluctuations that occur within the somata (these are restricted to somata and initial segments of processes arising from somata), (2) waves that occur exclusively within astrocyte processes and display repeated wave-like expansions and contractions of Ca^{2+}, and (3) microdomain Ca^{2+} fluctuations that display highly restricted areas in astrocyte processes. These do not expand or contract as waves and remain restricted. The distinct areas covered by these three types of fluctuations are reported in the main text and in **Supplementary Figure 5**. In this section, we describe a semi-automated method to accurately capture regions of interest (ROIs) for somatic, wave and microdomain Ca^{2+} fluctuations within astrocytes.

After an image series was acquired (for example, **Fig. 1**), the *x-y* axis drift in the image stacks was stabilized using the Turboreg plugin in ImageJ. All ROIs were then detected using GECIquant. A scale was first assigned to image stacks, based on the confocal digital zoom setting. For most images, we used a 3× digital zoom, which corresponds to a scale of 0.23 μm per pixel. Briefly, a temporal projection of the movie stack was thresholded and the soma was detected with an area criterion of 30 μm^2 to infinity within GECIquant. To do this, a temporal maximum intensity projection image was first generated by GECIquant from the image stack. The projection image was manually thresholded by the user with the default setting in ImageJ. Following thresholding, a polygon selection was manually drawn around the approximate astrocyte territory of interest, and the selection was added to the ImageJ ROI manager. Note that the assignment of territory was approximate and was not used for analysis except for the specific data set shown in **Figure 2b**. All ROIs falling within the range of 30 μm^2 to infinity inside the polygon selection were detected by GECIquant and added to the ROI manager. An area range of 30 μm^2 to infinity allowed detection of the astrocyte somata in all cases. The resulting detection was visually checked in every case.

To detect wave and microdomain ROIs, we first demarcated and deleted the soma from original image stacks using the clear selection feature in ImageJ. This was done because the increased basal fluorescence from the astrocyte soma relative to the processes prevented accurate thresholding of images for detection of ROIs in astrocyte processes. The ROI detection module in GECIquant was launched and the microdomain ROI option was selected. Microdomains and expanding wave ROIs were detected in separate analysis sessions. We used an area range of 0.5–4 μm^2 to detect microdomains and an area range of 5–2,000 μm^2 for waves. These values were chosen after initial examination of the movie frames and by using several initial 'best guess' test values as a guide. Other researchers who use GECIquant will also need to invest time initially to try several best guess values as a way to know what values will work best for the particular cell and fluctuation they are interested in measuring. The values we report here were appropriate for our experiments. For ROI detection, GECIquant generated a temporal maximum intensity projection image from the provided image stack with the deleted cell body. The projection image was manually thresholded by the user and a polygonal selection was manually drawn around the astrocyte of interest. GECIquant automatically detected microdomain and expanding wave ROIs based on the provided area criteria and the ROIs were added to the ImageJ ROI manager. Intensity values for each ROI were extracted in ImageJ and converted to dF/F values. For each ROI, basal F was determined during 50-s periods with no fluctuations. MiniAnalysis 6.0.07 (Synaptosoft) software was used to detect and measure amplitude, half width and frequency values for the somatic, wave and microdomain transients.

We comment on how we analyzed data for the experiments shown in **Figure 2**. First, for the analyses shown in **Figure 2c**, we made approximate ROIs that encompassed whole territories and then plotted the intensity of these regions over 300 s. From these traces, we measured the mean fluorescence intensity values over the 300-s period for each cell, and then averaged these values across all cells to generate the graphs in **Figure 2c** for WT and *Ip3r2*$^{-/-}$ mice. In the case of the graphs shown in **Figure 2d**, we pooled the individual microdomain and wave Ca^{2+} fluctuations per cell, obtained the average value per cell of these pooled fluctuations and repeated this procedure for all cells. Then we averaged across all cells to generate the graphs that are shown in **Figure 2c** for WT and *Ip3r2*$^{-/-}$ mice.

Graphs were made with Origin 8.1 and the figures assembled in CorelDraw 12 (Corel). No statistical methods were used to pre-determine sample sizes but our sample sizes are similar to those generally employed in the field. Randomization and blinding was not employed. Statistical comparisons were made using unpaired non parametric Mann-Whitney or unpaired parametric Student's *t* tests as deemed appropriate after analyzing the raw data to ascertain whether they were normally-distributed using the Dallal and Wilkinson approximation to Lilliefors' method within Instat. When a statistical test was used, the precise P value and the test employed are reported in the text and/or figures legends. If the P was less than 0.00001, then it is reported as $P < 0.00001$. Otherwise, precise P values are provided in each case.

A **Supplementary Methods Checklist** is available.

49. Madisen, L. *et al.* Transgenic mice for intersectional targeting of neural sensors and effectors with high specificity and performance. *Neuron* **85**, 942–958 (2015).
50. Pologruto, T.A., Sabatini, B.L. & Svoboda, K. ScanImage: flexible software for operating laser scanning microscopes. *Biomed. Eng. Online* **2**, 13 (2003).